



# Thermal analysis of an Eyring–Powell fluid peristaltic transport in a rectangular duct with mass transfer

Arshad Riaz<sup>1</sup>

Received: 19 March 2020 / Accepted: 16 April 2020 / Published online: 20 May 2020  
© Akadémiai Kiadó, Budapest, Hungary 2020

## Abstract

The present investigation establishes with analytical relevance for the thermal analysis in biological transport of Eyring–Powell fluid through a noncircular horizontal 3D channel. The relevant equations are physically exhibiting the problem under the lubrication mechanism. The wave frame analysis for the current study is considered to have a steady format of the problem. The resulting equations are presented with their analytic treatment by couple of series and closed-form techniques jointly. The aspects of different flow parameters are presented through plotting two- and three-dimensional curves of velocity expression, pressure gradient profile, peristaltic pressure data, temperature curves and mass distribution. The circulating bolus variation is also disclosed for the physical parameters to observe the stream lines pattern. It is observed from obtained graphical aspects that transfer of heat and mass is reduced for Eyring–Powell fluid model than a Newtonian fluid, but the same is enhanced with the aspect ratio of the three-dimensional rectangular channel.

**Keywords** Heat and mass transfer · Peristaltic flow · Eyring–Powell fluid · Rectangular channel · Analytical solutions

## Introduction

The most commonly used fluid models considered in engineering applications incorporate the Newtonian fluids; rather, large-scale analytical and experimental investigations have been presented for heat transfer behavior of Newtonian fluids [1–3]. However, in many industries including the chemical, pharmaceutical, biological and food industries, it is visualized to encounter non-Newtonian fluids depending on different stresses and viscosity models [4–6]. In [7], Waqas et al. have produced the theoretical data for Carreau–Yasuda nanofluid model by introducing thermal radiations and slip of the second order. They have also manipulated the impacts of chemical reaction and bioconvection and obtain the report that Weissenburg is reducing the flow velocity magnitude. Abolbashari et al. [8] talked about the modeling of Casson liquid with nanoparticles incursion and discussed the results for entropy generation through analytical approach. The study of Bhatti and Rashidi [9] came

for Williamson fluid to visualize the results of diffusion of heat along with radiation in the presence of nanoparticles through a porous shrinking and stretching sheet. They have applied the numerical methods to measure the readings. The model introduced by Eyring–Powell [10] somehow contains more complex mathematical structure, but it has certain benefits as compared with other viscoelastic fluid models. The kinetic theory of liquids is the origin of this model not the empirical expressions as most of the models make base. The Newtonian characteristics can also be derived from this model at low and large shear stress.

Recently, the study of peristaltic flows has achieved an immense concentration and interest of huge number of researchers due to their significant employments and application in many useful fields like physiology, engineering and the chemical factories. In the field of fluid mechanics, peristaltic flows of various types of viscous and nonlinear physical models have been suggested by a large number of physicists, mathematicians and engineering researchers by considering peristaltic pumping. A huge bit of literature is available for the study of such fluids under peristaltic motion [11–13]. To incorporate the wavy mechanism of viscoelastic stress models, the researchers have been predisposed in introducing different fluid models in various types of flow geometries. Most of the containers adjusted in industries

✉ Arshad Riaz  
arshad-riaz@ue.edu.pk

<sup>1</sup> Department of Mathematics, Division of Science and Technology, University of Education, Lahore 54770, Pakistan

and clinical laboratories are exhibiting three dimensions in space. To discuss the behavior of peristaltic transport in certain geometries having space frame of references, a small number of researchers are motivated to deal with rectangular channels and cylinders. Reddy et al. [14] proposed the influence of moving sides on a fluid in a Cartesian peristaltic conduit and concluded the theory that the straight transactional side of the uterus is preferably observed by an enclosure of rectangular faces besides a channel with a two-coordinate system. Mekheimer et al. [15] have investigated the eccentricity of two cylinders with peristaltic transport mathematically. Stokesian peristaltic mechanism in a three-dimensional asymmetric tube is unveiled in [16]. Aranda et al. [17] talked about the Stokesian peristaltic scheme in a closed three-dimensional tube and executed the observation that 3D flexible tube is affecting the results of the peristaltic pumping through its closed ends and the way the peristaltic waves blow toward outside the cavity. Abbas et al. [18] have utilized the outcomes of nonuniform three-dimensional geometry with elastic walls for the wavy mechanism of Tangent hyperbolic fluid and developed the result that fluid travels relatively slower in due to walls compliance. It can be found in the literature that only a few studies have been reported on the pumping flow of viscoelastic fluids in three-dimensional Cartesian channels. The wide range of its applications and benefits in clinical and engineering perspectives emphasizes that this geometry must be more discussed for various models of the physical fluids.

In the field of peristaltic wonders, incorporations of thermal and mass exchange have been examined by numerous specialists. Nadeem et al. [19] introduced thermal blood analysis in a diverging tube for third-grade fluid. The relation among wavy structure with heat exchange over movement of a viscous liquid in a bidimensional magnetized and porous channel is assumed in [20]. Ogulu [21] analyzed thermal and concentration change phenomenon of blood through a solitary lymphatic vein under a uniform magnetized environment. Mekheimer and Abd Elmaboud [22] dissected the heat impact with magnetic field on pumping terminology of a viscous liquid across a vertically oriented annulus through lubrication assumptions. In the studies of three-dimensional thermally conducting mass transfer flows, most of the time the observing representative conservation equations become linear/nonlinear partial differential equations or more specifically coupled system of three equations which cannot be tackled by exact methods. In such situations, the most appropriate analytical technique to be used is homotopy perturbation method firstly introduced by He [23, 24] which was efficiently implemented for nonlinear ordinary differential equations.

To the best of authors' information, the subject of thermal impacts and mass exchange attributes on peristaltic stream of Eyring–Powell liquid in a duct segment is yet to break down.

Remembering the above conversation, we chose to explore the investigation of thermal and mass transfer examination for the peristaltic stream of Eyring–Powell liquid model in a three-dimensional cross-area of a rectangular duct. The constitutive set of equations are formatted within the sight of small wave amplitude and negligible Reynolds number presumptions with the analytical arrangements produced through homotopy perturbation method by using the method of eigenfunction. On the other hand, the data of pressure rise are interpolated through numerical treatment. The subsequent information is used to examine the graphical highlights of every relevant parameter showing up in the examination. The flow pattern is additionally shown through streamlines.

## Mathematical formulation

Let us approach the wavy-type flow in a cross-face of Cartesian channel with three faces containing the non-Newtonian Eyring–Powell fluid under the environment of thermal and mass exchange. The width of the section is  $2d$ , and the altitude is  $2a$  which can be viewed in Fig. 1. The geometrical suppositions are as follows: The temperatures  $T_0, T_1$  and mass concentrations  $C_0, C_1$  are assigned to the horizontal sides of the channel, correspondingly. The upward and downward oriented boundaries are assumed to create long peristaltic waves as compared to the amplitude.

Mathematically, the walls suggest the relations [14]

$$Z = f'(X, t') = \pm \left( a + \frac{1}{b^{-1} \sec \left( \frac{2\pi}{\lambda(X-ct')^{-1}} \right)} \right).$$

Here, the wave amplitude is given by  $b$ ,  $\lambda$  is showing the wavelength,  $c$  gives speed with which wave is propagated,  $t$  chooses the time measurements and  $x$  exhibits the wave

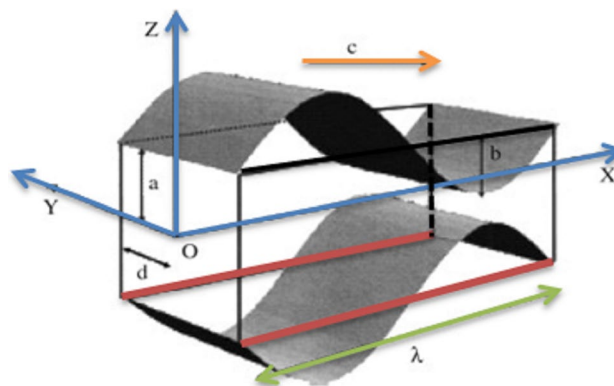


Fig. 1 Geometrical structure of the container

direction. The walls normal to  $y$ -axis do not contribute in creating waves due to their stable manufacturing. The constitutive model of fluid taken is described by [10]

$$\begin{aligned} \mathbf{S} &= \mu \text{grad} \mathbf{V}' + \frac{1}{\beta_1} \arcsin h(c_1^{-1} \text{grad} \mathbf{V}'), \\ \sinh^{-1}(c_1^{-1} \text{grad} \mathbf{V}') &\approx c_1^{-1} \text{grad} \mathbf{V}' \\ &-\frac{1}{6}(c_1^{-1} \text{grad} \mathbf{V}')^3, \quad |c_1^{-1} \text{grad} \mathbf{V}'|^5 \leq 1, \end{aligned} \tag{1}$$

where the viscosity is suggested by  $\mu$ , while  $\beta$  and  $c_1$  are the fluid material representatives. Let  $\mathbf{V}' = U\mathbf{i} + W\mathbf{k}$  be the fluid velocity vector for current flow. The flow is governed by the conservation laws described through their mathematical form below:

$$\partial_x U + \partial_z W = 0, \tag{2}$$

$$\rho(\partial_t U + U * \partial_x U + W * \partial_z U) + \partial_x P = \partial_x S_{xx} + \partial_y S_{xy} + \partial_z S_{xz}, \tag{3}$$

$$\partial_y P = \partial_x S_{yx} + \partial_y S_{yy} + \partial_z S_{yz}, \tag{4}$$

$$\begin{aligned} \rho(\partial_t W + U * \partial_x W + W * \partial_z W) + \partial_z P \\ = \partial_x S_{zx} + \partial_y S_{zy} + \partial_z S_{zz}, \end{aligned} \tag{5}$$

$$\begin{aligned} C'(\partial_t T + U * \partial_x T + W * \partial_z T) &= \frac{K'}{\rho}(\partial_{xx} T + \partial_{yy} T + \partial_{zz} T) \\ &+ \frac{1}{\rho}(S_{xy} \partial_y U + S_{xz} \partial_z U), \end{aligned} \tag{6}$$

$$\begin{aligned} (\partial_t C + U * \partial_x C + W * \partial_z C) &= D(\partial_{xx} C + \partial_{yy} C + \partial_{zz} C) \\ &+ \frac{DK_T}{T_m}(\partial_{xx} T + \partial_{yy} T + \partial_{zz} T). \end{aligned} \tag{7}$$

The above-mentioned parameters are such that  $K'$  represents the thermal conductivity,  $C'$  shows the specific heat,  $T_m$  gives the average temperature,  $K_T$  suggests the thermal–diffusion ratio and  $D$  predicts the mass diffusibility coefficient. Transforming the coordinates into a new coordinate system of a newly taken wave frame, we relate through the following transformations:

$$(x', y', z', u', w', p') = (X - ct', Y, Z, U - c, W, P). \tag{8}$$

Suggesting the subsequent dimensionless strategy, we obtain

$$\begin{aligned} \bar{x} &= \lambda^{-1} x', \quad \bar{y} = d^{-1} y', \quad \bar{z} = a^{-1} z', \\ \bar{u} &= c^{-1} u', \quad \bar{w} = (\delta c)^{-1} w', \quad \bar{t} = \lambda^{-1} ct', \quad \bar{h} = a^{-1} h, \\ \bar{p} &= \frac{a^2 p'}{\mu c \lambda}, \quad \theta = \frac{T - T_0}{T_1 - T_0}, \quad \sigma = \frac{C - C_0}{C_1 - C_0}, \\ \text{Re} &= \frac{\rho a c}{\mu}, \quad \delta = \frac{a}{\lambda}, \quad \phi = \frac{b}{a}, \quad \bar{S} = \frac{a}{\mu c} S, \quad \beta = \frac{a}{d}, \\ M_1 &= \frac{1}{\mu \beta_1 c_1}, \quad K = \frac{M_1 c^2}{6 c_1^2 a^2}, \quad P_r = \frac{\mu C'}{K'}, \\ E_c &= \frac{c^2}{C'(T_1 - T_0)}, \quad S_c = \frac{\mu}{\rho D}, \quad S_r = \frac{\rho D K_T (T_1 - T_0)}{\mu T_m (C_1 - C_0)}. \end{aligned} \tag{9}$$

The amounts  $M_1$  and  $K$  hint the non-dimensional quantities of the liquid. Joining the dimensionless amounts with the relations (2)–(7) and utilizing the requirements of laminarity of the stream ( $\text{Re} \rightarrow 0$ ) and small amplitude ( $\lambda \rightarrow \infty$ ) approximations, the final form of the upcoming flow equations (in the wake of skipping the bars) in newly introduced frame can be separately composed as:

$$\partial_x u + \partial_z w = 0, \tag{10}$$

$$\begin{aligned} \beta^2 \partial_{yy} u + \partial_{zz} u - \frac{3K}{1 + M_1} (\beta^4 (\partial_y u)^2 \partial_{yy} u \\ + (\partial_z u)^2 \partial_{zz} u) = \frac{1}{1 + M_1} \partial_x p, \end{aligned} \tag{11}$$

$$\begin{aligned} \beta^2 \partial_{yy} \theta + \partial_{zz} \theta + P_r E_c ((1 + M_1) (\beta^2 (\partial_y u)^2 \\ + (\partial_z u)^2) - K (\beta^4 (\partial_y u)^4 + (\partial_z u)^4)) = 0, \end{aligned} \tag{12}$$

$$\beta^2 \partial_{yy} \sigma + \partial_{yy} \sigma + S_r S_c (\beta^2 \partial_{yy} \theta + \partial_{zz} \theta) = 0. \tag{13}$$

In the above expression,  $P_r$  shows the Prandtl number,  $E_c$  gives the Eckert number,  $S_r$  means the Soret number and  $S_c$  depicts the Schmidt number. The concerning dimensionless surface conditions for the considered scenario are stated as [14]:

$$u(\mp 1, z) + 1 = 0 \text{ and } u(y, \mp h(x)) + 1 = 0 \text{ with } h(x) = 1 + \phi * \cos 2\pi x, \tag{14}$$

$$\theta = \begin{cases} 0 & \text{at } z = h \\ 1 & \text{at } z = -h \end{cases}, \tag{15}$$

$$\sigma = \begin{cases} 0 & \text{at } z = h \\ 1 & \text{at } z = -h \end{cases}. \tag{16}$$

It is to be mentioned here that the above-discussed problem relates to the two-dimensional channel when  $\beta \rightarrow 0$  and  $\beta = 1$  generates the square shape duct readings. It can also be

analyzed that limiting  $K$  and  $M_1$  to zero regenerates properties of linear fluid.

## Solution strategy

The finalized sets of equations (11) and (15) are being handled by HPM [23, 24]. The homotopy for the unknown profiles mentioned in the above equations is structured as:

$$L_{\text{vel}}(u - \hat{u}_0) + q \left[ L_{\text{vel}}(u) - 3K(1 + M_1)^{-1} \left( \beta^4 \left( \frac{\partial u}{\partial y} \right)^2 \frac{\partial^2 u}{\partial y^2} + \left( \frac{\partial u}{\partial z} \right)^2 \frac{\partial^2 u}{\partial z^2} \right) - \frac{1}{1 + M_1} \frac{\partial p}{\partial x} \right] = 0, \quad (17)$$

$$L_{\text{temp}}(\bar{\theta} - \hat{\theta}_0) + q \left[ L_{\text{temp}}(\bar{\theta}) + \beta^2 \frac{\partial^2 \bar{\theta}}{\partial y^2} + P_r E_c \left( (1 + M_1) \left( \beta^2 \left( \frac{\partial u}{\partial y} \right)^2 + \left( \frac{\partial u}{\partial z} \right)^2 \right) - K \left( \beta^4 \left( \frac{\partial u}{\partial y} \right)^4 + \left( \frac{\partial u}{\partial z} \right)^4 \right) \right] = 0. \quad (18)$$

For further analogy, we have taken  $L_{\text{vel}} = \beta^2 \frac{\partial^2}{\partial y^2} + \frac{\partial^2}{\partial z^2}$  and  $L_{\text{temp}} = \frac{\partial^2}{\partial z^2}$  as the linear operators. The initial approximations are chosen as:

$$\hat{u}_0(y, z) = \frac{1 - y^2 + \beta^2(z^2 - h^2 - 1)}{\beta^2}, \quad \hat{\theta}_0 = \frac{1 - z/h}{2}. \quad (19)$$

Applying perturbation on the involved parameter  $q$  for the variables  $u$  and  $\theta$ , we have

$$u = u_0 + qu_1 + q^2u_2 + \dots \quad (20)$$

$$\bar{\theta} = \theta_0 + q\theta_1 + q^2\theta_2 + \dots \quad (21)$$

Injecting expressions (20) and (21) into relations (17) and (18) and then composing the terms involving coefficients of nonnegative increasing integral powers of  $q$ , we collect

$$L_{\text{vel}}(u_0) - L_{\text{vel}}(\hat{u}_0) = 0, \quad (22)$$

$$u_0 + 1 = 0 \text{ when } y \pm 1 = 0, \quad u_0 + 1 = 0 \text{ when } z \pm h(x) = 0, \quad (23)$$

$$L_{\text{temp}}(\theta_0) - L_{\text{temp}}(\hat{\theta}_0) = 0, \quad (24)$$

$$\theta_0 = 0 \text{ at } z = h(x), \quad \theta_0 = 1 \text{ at } z = -h(x). \quad (25)$$

From Eqs. (19) and (22–25), we gain the following results:

$$u_0 = \hat{u}_0(y, z) = -1 + \frac{1}{\beta^2}(1 - y^2) + z^2 - h^2(x), \quad (26)$$

$$\theta_0 = \hat{\theta}_0 = \frac{h(x) - z}{2h(x)},$$

$$\beta^2 \frac{\partial^2 u_1}{\partial y^2} + \frac{\partial^2 u_1}{\partial z^2} - \frac{3K}{1 + M_1} \left( \beta^4 \left( \frac{\partial u_0}{\partial y} \right)^2 \frac{\partial^2 u_0}{\partial y^2} + \left( \frac{\partial u_0}{\partial z} \right)^2 \frac{\partial^2 u_0}{\partial z^2} \right) - \frac{1}{1 + M_1} \frac{\partial p}{\partial x} = 0, \quad (27)$$

$$u_1 = 0 \text{ when } y = \pm 1 \text{ and } u_1 = 0 \text{ when } z = \pm h(x), \quad (28)$$

$$\frac{\partial^2 \theta_1}{\partial z^2} + \beta^2 \frac{\partial^2 \theta_1}{\partial y^2} + P_r E_c \left( (1 + M_1) \left( \beta^2 \left( \frac{\partial u_0}{\partial y} \right)^2 + \left( \frac{\partial u_0}{\partial z} \right)^2 \right) - K \left( \beta^4 \left( \frac{\partial u_0}{\partial y} \right)^4 + \left( \frac{\partial u_0}{\partial z} \right)^4 \right) \right) = 0, \quad (29)$$

$$\theta_1 = 0 \text{ when } y = \pm 1, \quad \theta_1 = 0 \text{ when } z = \pm h(x). \quad (30)$$

Now, switching the eigenfunction expansion technique on Eq. (27), the closed form of  $u_1$  can be observed as follows:

$$u_1 = \sum_{n=1}^{\infty} a_n(y) \cos(2n - 1) \frac{\pi}{2h(x)} z, \quad (31)$$

where  $a_n(y)$  is summarized as:

$$\begin{aligned}
 a_n(y) = & \left( 4 \cos(n\pi) (\cosh(\lambda'_n) - \sinh(\lambda'_n)) \left( -1(1 - 2n)^2 \frac{dp}{dx} \pi^2 (\beta \lambda_n)^2 - 24K \right. \right. \\
 & \left. \left( -8h^2(x) (\beta \lambda_n)^2 + [\pi(1 - 2n)]^2 (-2\beta^2 - \lambda_n^2 + h^2(x) (\beta \lambda_n)^2) \right) \right) \left( \cosh\left(\frac{\lambda_n}{\beta}\right) - \sinh\left(\frac{\lambda_n}{\beta}\right) \right) \\
 & + \left( (1 - 2n)^2 \frac{dp}{dx} \pi^2 (\beta \lambda_n)^2 + 24K (-8h(x)^2 (\beta \lambda_n)^2 + \pi^2 (1 - 2n)^2 (-2\beta^2 - \lambda_n^2 + h^2(x) \right. \right. \\
 & \left. \left. (\beta \lambda_n)^2) \right) (\cosh(\lambda'_n) - \sinh(\lambda'_n)) + \left( (1 - 2n)^2 \frac{dp}{dx} \pi^2 (\beta \lambda_n)^2 + 24K (-8h^2(x) \right. \right. \\
 & \left. \left. (\beta \lambda_n)^2 + \pi^2 (1 - 2n)^2 (-2\beta^2 - \lambda_n^2 + h^2(x) (\beta \lambda_n)^2) \right) \right) \left( \cosh\left(\frac{2\lambda_n}{\beta} + \lambda'_n\right) - \right. \\
 & \left. \sinh\left(\frac{2\lambda_n}{\beta} + \lambda'_n\right) \right) + \left( (1 - 2n)^2 \frac{dp}{dx} \pi^2 (\beta \lambda_n)^2 - 24K (-8h^2(x) (\beta \lambda_n)^2 + \pi^2 (1 - 2n)^2 \right. \\
 & \left. (-2\beta^2 - \lambda_n^2 + h^2(x) (\beta \lambda_n)^2) \right) \left( \cosh\left(\frac{\lambda_n}{\beta} + 2\lambda'_n\right) + \sinh\left(\frac{\lambda_n}{\beta} + 2\lambda'_n\right) \right) \\
 & / \left( (1 + M_1) (2n - 1)^3 \pi^3 \beta^2 \lambda_n^4 \left( 1 + \cosh\left(\frac{2\lambda_n}{\beta}\right) + \sinh\left(\frac{2\lambda_n}{\beta}\right) \right) \right).
 \end{aligned} \tag{32}$$

Here,  $\lambda_n = (2n - 1)\pi/2h(x)$ ,  $n \in Z^+$  suggest the eigenvalues and  $\lambda'_n = \frac{\lambda_n y}{\beta}$ . The expression of temperature profile is evaluated as:

$$u = u_0 + u_1 + \dots \tag{34}$$

$$\theta = \theta_0 + \theta_1 + \dots \tag{35}$$

$$\begin{aligned}
 \theta_1 = & \frac{1}{105\beta^6} 8E_c K (1 + M_1) P_r (420y^6(z^2 - h(x)^2) + 70y^4(z^4 - h(x)^4)\beta^2 \\
 & + 28y^2(z^6 - h(x)^6)\beta^4 + 15(z^8 - h(x)^8)\beta^6).
 \end{aligned} \tag{33}$$

The closed-form series solution of concentration profile can be calculated from Eq. (13) along with boundary conditions (16) and is found as:

The particular complete solutions are achieved when  $q \rightarrow 1$  which are observed as:

$$\sigma = f(x, y, z) + \sum_{n=1}^{\infty} \left( c_n \cosh\left(\frac{\lambda_n}{\beta} y\right) + d_n \sinh\left(\frac{\lambda_n}{\beta} y\right) \right) \cos(\lambda_n z), \tag{36}$$

where

$$\begin{aligned}
 f(x, y, z) = & \frac{1}{240h(x)(x, t)\beta^6} (h(x) - z) (105\beta^6 - 64E_c h(x) K (1 + M_1) P_r S_c S_r (h(x) + z) \\
 & (-105y^6 + 35y^4 (37h(x)^2 - 8z^2) \beta^2 + 7y^2 (13h(x)^4 - 2h(x)^2 z^2 - 2z^4) \beta^4 \\
 & + (3h(x)^6 - 4h(x)^4 z^2 - 4h(x)^2 z^2 - 4z^6) \beta^6)), \\
 c_n = & \frac{-1}{(2n - 1)^9 \pi^9 \beta^6} \left( 2 \operatorname{sech}\left(\frac{\lambda_n}{\beta}\right) \left( (a_2 + b_2 - 1) (1 - 2n)^8 \pi^8 \beta^6 - 512E_c h(x)^2 K (1 + M_1) \right. \right. \\
 & P_r S_c S_r (-49152h(x)^6 \beta^6 + 768h(x)^4 (1 - 2n)^2 \pi^2 \beta^4 (y^2 + 8h(x)^2 \beta^2) + (1 - 2n)^6 \pi^6 \\
 & (y^2 + h(x)^2 \beta^2) (y^4 + h(x)^4 \beta^4) - 32h(x)^2 (1 - 2n)^4 \pi^4 \beta^2 (4y^4 + 3h(x)^2 y^2 \beta^2 \\
 & \left. \left. + 4h(x)^4 \beta^4 \cos(n\pi) \right) \right)
 \end{aligned}$$

and

$$d_n = \frac{2(b_2 - a_2) \cos[n\pi] \cos\left(\frac{\lambda_n}{\beta}\right)}{(2n - 1)\pi}$$

The volumetric flow rate  $\bar{F}$  is calculated as:

$$\bar{F} = \int_0^{h(x)} \int_0^1 u(x, y, z) dy dz \tag{37}$$

The instantaneous flux is found by

$$\bar{Q} = \int_0^h \int_0^1 (u + 1) dy dz = \bar{F} + h(x) \tag{38}$$

The average value of volumetric rate of flow per single wave circulation is defined by

$$Q = \frac{\int_0^T \bar{Q} dt}{T} = \bar{F} + 1, \quad \bar{T} \text{ being assumed the time period.} \tag{39}$$

The pressure profile  $dp/dx$  is extracted through entertaining results (37) and (39) which is composed as:

$$\begin{aligned} \frac{dp}{dx} = & \left( -(1 + M_1)(2n - 1)^4 \pi^2 \lambda_n^3 \left( 1 + \cosh(2\lambda_n \beta^{-1}) + \sinh\left(\frac{2\lambda_n}{\beta}\right) \right) \left( \frac{-2h(x)^3}{3} - Q + \frac{2h(x)}{3\beta^2} \right) \right. \\ & + \left[ (1 + M_1)(2n - 1)^4 \pi^2 \beta^2 \lambda_n^5 \left( 1 + (\cosh + \sinh)\left(\frac{2\lambda_n}{\beta}\right) \right) \right]^{-1} (64h(x)K(-24h(x)^2 \beta^2 \lambda_n^2 \\ & \left( -\beta + (\beta - \lambda_n) \cosh\left(\frac{2\lambda_n}{\beta}\right) + (\beta - \lambda_n) \sinh\left(\frac{2\lambda_n}{\beta}\right) \right) + \pi^2(-2n + 1)^2 (\lambda_n^3 \\ & \left( 1 + \cosh\left(\frac{2\lambda_n}{\beta}\right) + \sinh\left(\frac{2\lambda_n}{\beta}\right) \right) + (3\beta^3 (h(x)^2 \lambda_n^2 - 2) - 3\beta \lambda_n^2) \left( -1 + \cosh\left(\frac{2\lambda_n}{\beta}\right) \right. \\ & \left. \left. + \sinh\left(\frac{2\lambda_n}{\beta}\right) \right) - 3\beta^2 \lambda_n (h(x)^2 \lambda_n^2 - 2) \left( 1 + \cosh\left(\frac{2\lambda_n}{\beta}\right) + \sinh\left(\frac{2\lambda_n}{\beta}\right) \right) \right) \right) \\ & \left. / (8h(x)(1 - 2n)^2 ( (\beta - \lambda_n) - (\beta + \lambda_n) \cosh\left(\frac{2\lambda_n}{\beta}\right) + (\beta - \lambda_n) \sinh\left(\frac{2\lambda_n}{\beta}\right) \right) \right) \end{aligned} \tag{40}$$

The pressure rise  $\Delta p$  is found by numerical integration on Mathematica by making use of the integral below:

$$\Delta p = \int_0^1 \left( \frac{dp}{dx} \right) dx \tag{41}$$

### Graphical investigations

In this portion of the article, we explained the results manipulated graphically for velocity, pressure rise, pressure gradient, temperature distribution, concentration profile and stream functions to discuss the contribution of pertinent parameters. Tables are also presented to watch out the numerical variation in the profiles of velocity, temperature and concentration for Newtonian and non-Newtonian Eyring–Powell model. Tables 1, 2 and 3 correspond to the variations of velocity  $u$ , temperature  $\theta$  and concentration  $\sigma$ , respectively. The velocity profile  $u$  is sketched in Figs. 2–4 against the space coordinate  $z$  under the alteration of the parameters  $\beta$ ,  $K$  and  $M_1$  for both two and three dimensions. Figures 5–7 are displayed to consider the behavior of pressure rise curve  $\Delta p$  for  $\beta$ ,  $M_1$  and  $\phi$ . The variational distribution of  $dp/dx$  is revealed in Figs. 8–11 to depict the influence of the quantities  $\beta$ ,  $K$ ,  $M_1$  and  $Q$ . The temperature distribution  $\theta$  is shown in Figs. 12–14 under the variation of  $\beta$ ,  $E_c$  and  $M_1$ , respectively. Figures 15–17 imply the effects of  $\beta$ ,  $S_c$  and  $M_1$  on mass concentration distribution. The stream functions are portrayed in Figs. 18–20 to examine the small rounded mass (called bolus) shape phenomenon.

Figure 2(a,b) shows the readings of velocity profile  $u$  under the parameter  $\beta$ . It is to be mentioned here that

velocity is increasing when we enlarge the magnitude of  $\beta$ . The treatment of velocity field for the parameter  $K$  is examined from Fig. 3a, b. We can depict here that the velocity is diminishing with the monotonic changes in  $K$  by keeping all other quantities constant. From Fig. 4a, b, it is admitted that the profile is varying linearly with the small values of  $M_1$ , but as we give larger magnitude to the parameter  $M_1$ , the velocity curves are coming near to each other.

Figure 5 indicates the alteration of pressure rise curves  $\Delta p$  for the parameter  $\beta$ . It is convincing that the pressure rise is

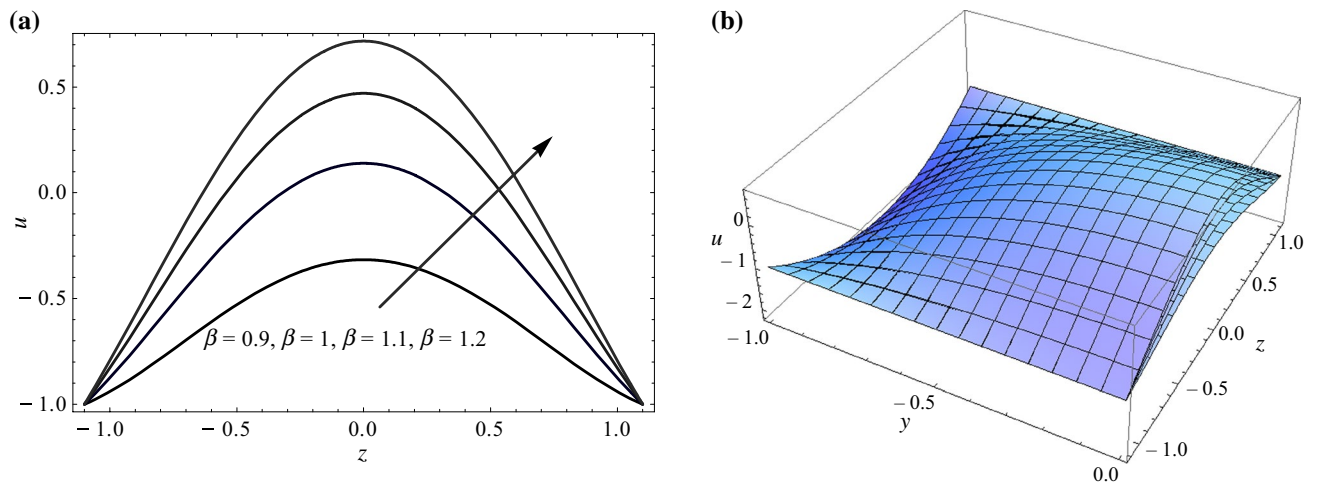


Fig. 2 Horizontal velocity against  $\beta$  a 2D b 3D

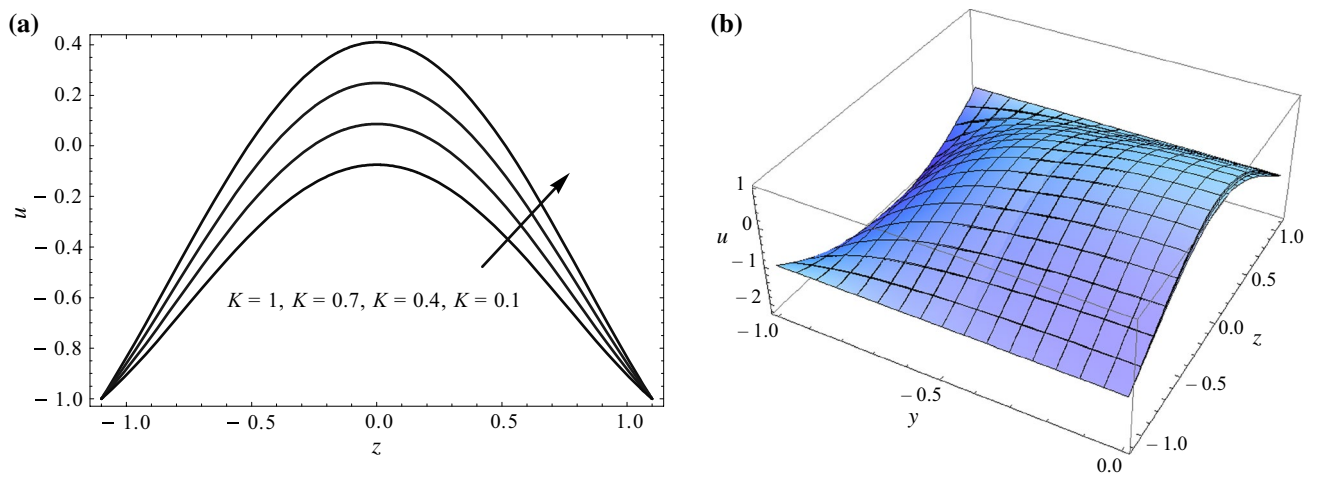


Fig. 3 Horizontal velocity against  $K$  a 2D b 3D

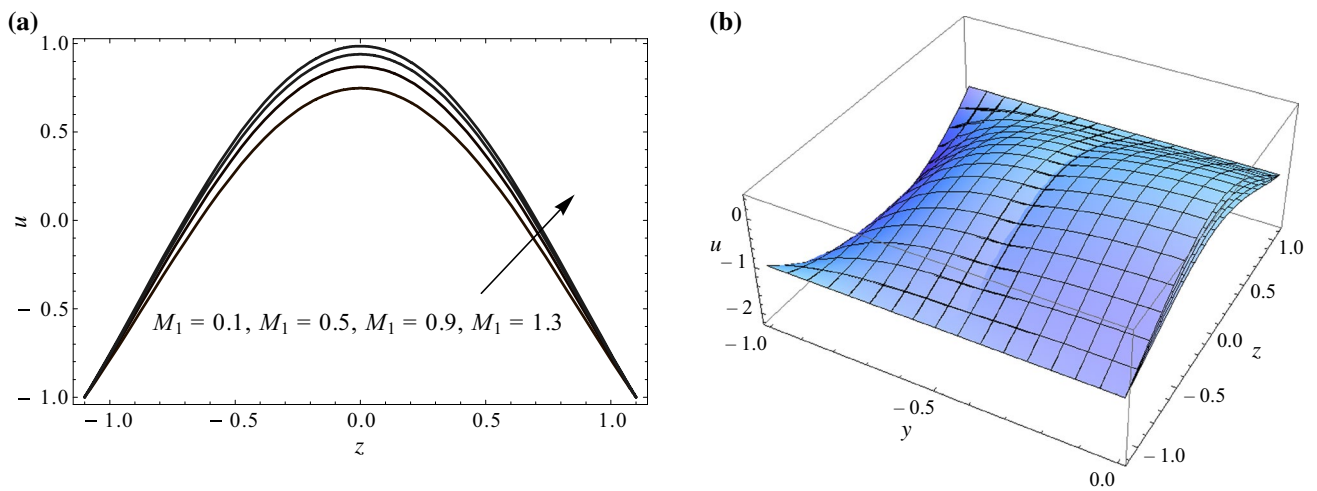


Fig. 4 Horizontal velocity against  $M_1$  a 2D b 3D

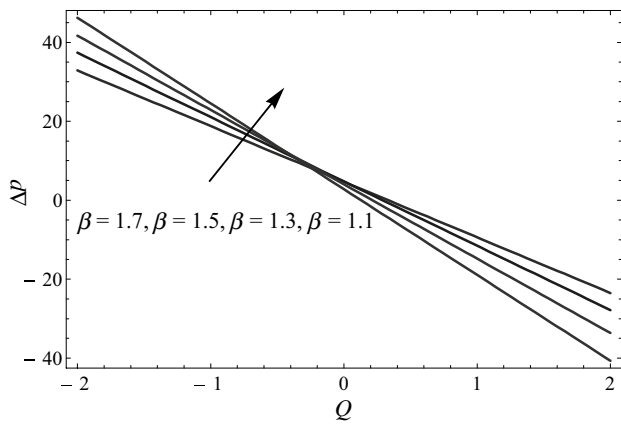


Fig. 5 Pressure rise curves  $\Delta p$  against  $\beta$

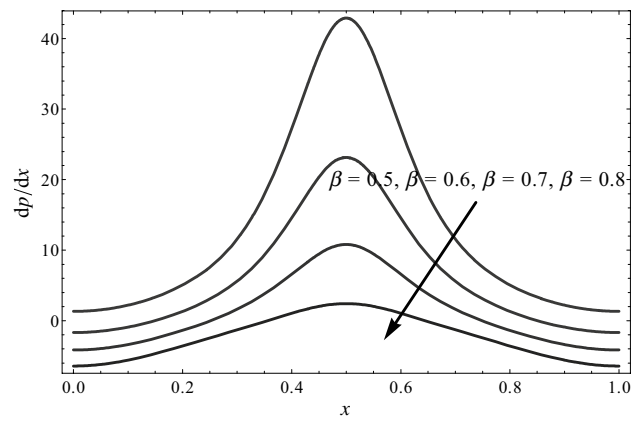


Fig. 8 Pressure gradient  $dp/dx$  against  $\beta$

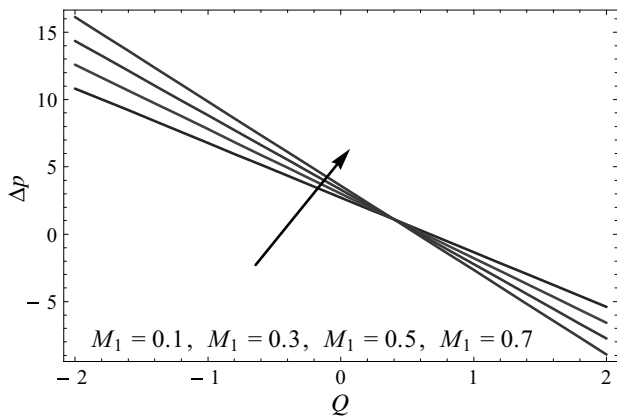


Fig. 6 Pressure rise curves  $\Delta p$  against  $M_1$

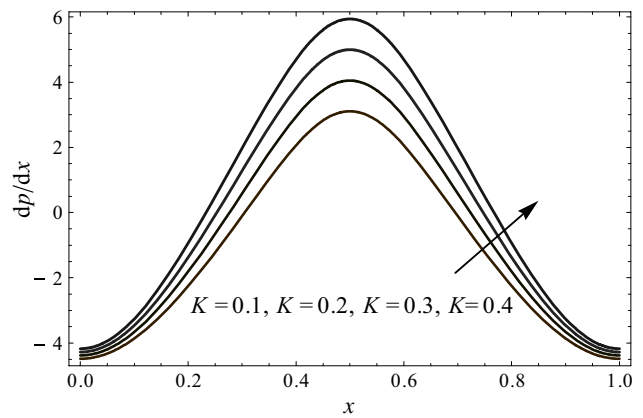


Fig. 9 Pressure gradient  $dp/dx$  against  $K$

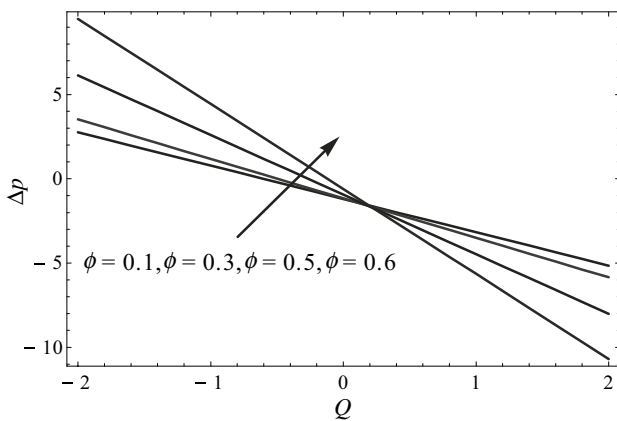


Fig. 7 Pressure rise curves  $\Delta p$  against  $\phi$

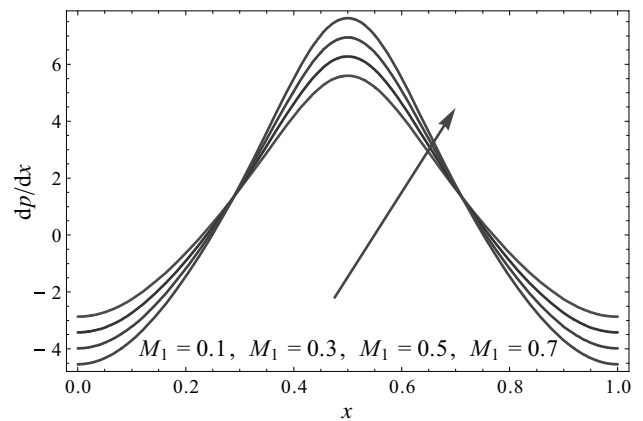


Fig. 10 Pressure gradient  $dp/dx$  against  $M_1$



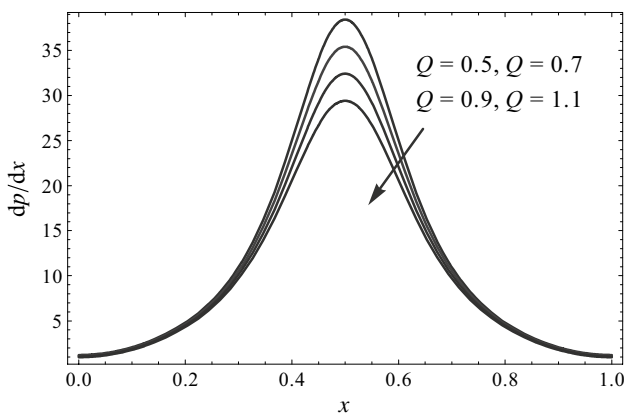


Fig. 11 Pressure gradient  $dp/dx$  against  $Q$

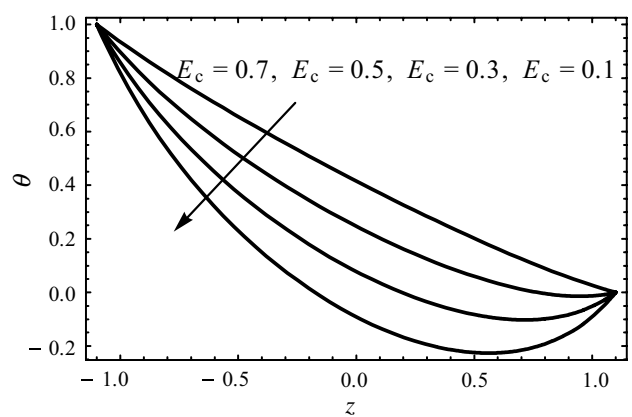


Fig. 13 Temperature distribution  $\theta$  against  $E_c$

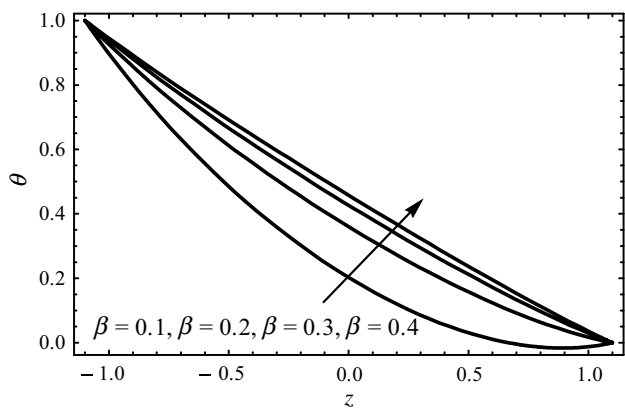


Fig. 12 Temperature distribution  $\theta$  against  $\beta$

decreasing with the increase in  $\beta$  in the retrograde pumping region ( $\Delta p > 0 > Q$ ), while inverse scenario is reported in the pumping portion ( $\Delta p, Q > 0$ ) and augmented pumping region ( $\Delta p, Q < 0$ ). We can describe through Fig. 6 that pressure rise  $\Delta p$  is varying linearly with the change of parameter  $M_1$  in the retrograde pumping as well as peristaltic pumping areas, while reverse behavior is measured in the copumping region. The impact of pressure rise profile against the flow rate  $Q$  for the parameter  $\phi$  is displayed in Fig. 7. One can observe that the attitude of pressure rise distribution for  $\phi$  is quite parallel to that of the parameter  $M_1$ .

To see the pressure gradient distribution  $dp/dx$  against the parameter  $\beta$ , Fig. 8 is shown. Here, we can suggest that pressure gradient gives the inverse behavior when someone

increases the contribution of  $\beta$ . It is also resulted that much pressure gradient is examined in the middle of the channel, while in the corner regions, the pressure gradient has a minimum width. It shows that extensive amount of pressure change is required in the central part to balance the flow relative to the walls of the channel. Figure 9 deliberates that the pressure gradient  $dp/dx$  chooses the linear relation with the parameter  $K$  and pressure gradient curves become much closer to each other imminent to the walls. The influence of parameter  $M_1$  on pressure gradient profile  $dp/dx$  is shown in Fig. 10. One observes that the pressure gradient is increasing with the increase in  $M_1$  in the region  $x \in [0.3, 0.7]$ , while inverse investigation is made in the rest of the region. Figure 11 discloses the variation of pressure gradient  $dp/dx$  with the flow rate  $Q$ . It is measured that pressure gradient is lessening with the flow rate and it becomes nominal at the nook of the domain.

Figure 12 shows the variation of temperature distribution  $\theta$  for the parameter  $\beta$ . It is mentioned here that temperature profile is getting larger while increasing the values of  $\beta$ . It is also noted here that the temperature curves are getting nearby to each other. Figure 13 ensures that the temperature distribution  $\theta$  is linearly proportional to the Eckert number  $E_c$ . One can observe the variation of temperature profile  $\theta$  against the parameter  $M_1$  from Fig. 14 and can be seen that as we increase the values of  $M_1$ , the temperature curves are reducing their height. Figure 15 shows the variation of concentration profile  $\sigma$  with the effect of aspect ratio  $\beta$ . It is derived from this figure that the more the aspect ratio, the larger

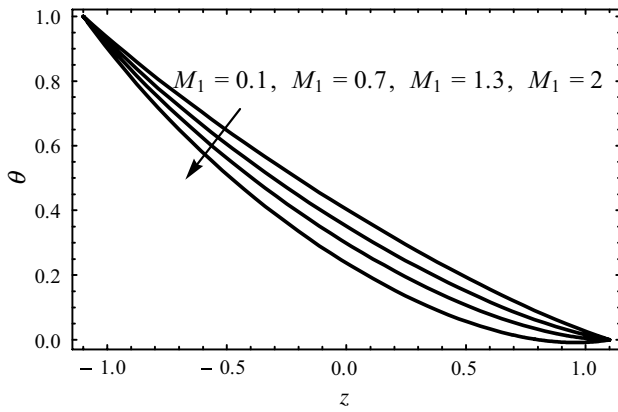


Fig. 14 Temperature distribution  $\theta$  against  $M_1$

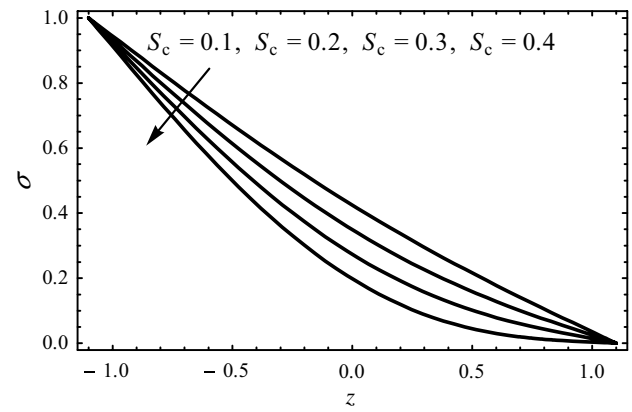


Fig. 16 Mass concentration  $\sigma$  against  $S_c$

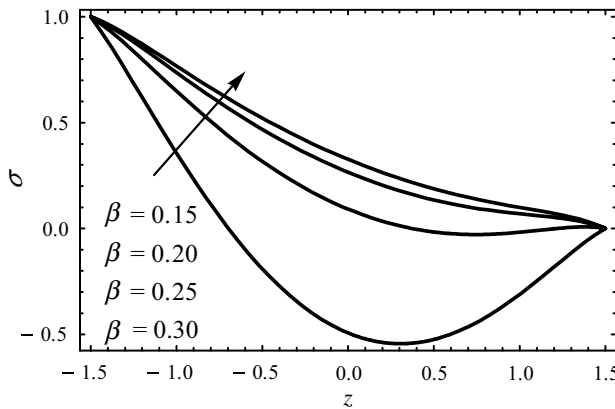


Fig. 15 Mass concentration  $\sigma$  against  $\beta$

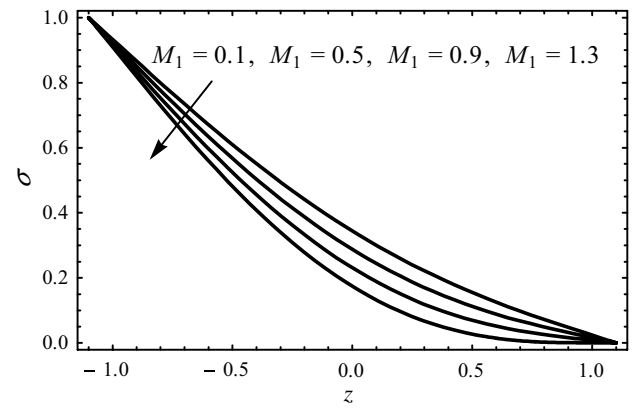


Fig. 17 Mass concentration  $\sigma$  against  $M_1$

the concentration and more variation is seen in the middle of the channel as compared to the corners. It is depicted from Figs. 16 and 17 that concentration curves are varying inversely to the change in Schmidt number  $S_c$  and the fluid parameter  $M_1$  but is also observed that concentration profile is depending on Schmidt number more than that of  $M_1$ .

In Fig. 18, the streamlines are appeared to observe the flow phenomenon in rectangular channel for the parameter  $\beta$ . It is observed that the number of trapping bolus is enhanced

with rising intensity of  $\beta$ , while dimensions of the bolus are varying under the exceeding values of  $\beta$ . To see the streamlines for the parameter  $K$ , Fig. 19 is presented. It is concluded from this graph that trapping boluses are contracted in size but do not change their quantity while we give large values to  $K$ . From Fig. 20, one can estimate that trapping boluses remain the same in number and dimensions when  $M_1 \leq 1$  but decrease in magnitude and volume when  $M_1 > 1$ .

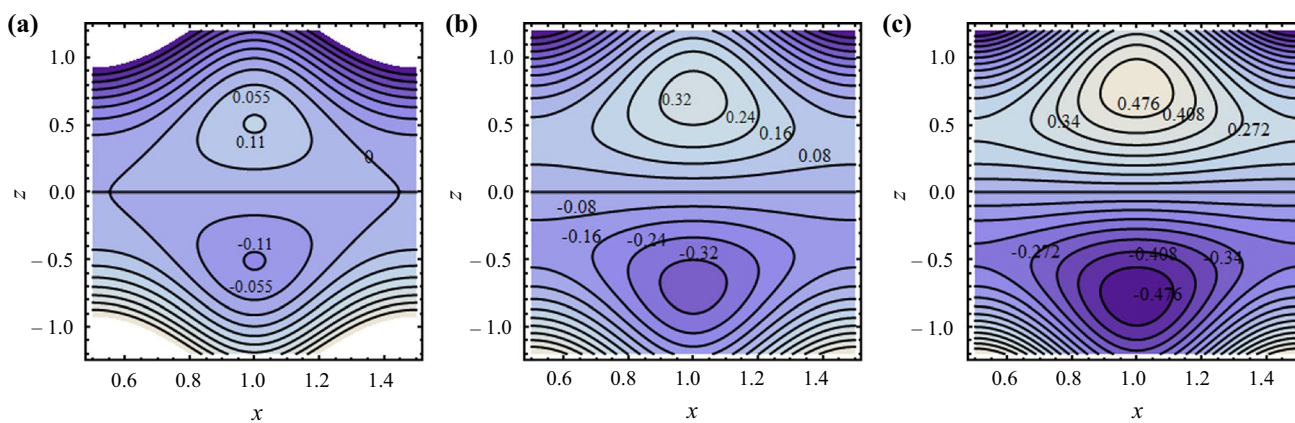


Fig. 18 Streamlines against  $\beta$

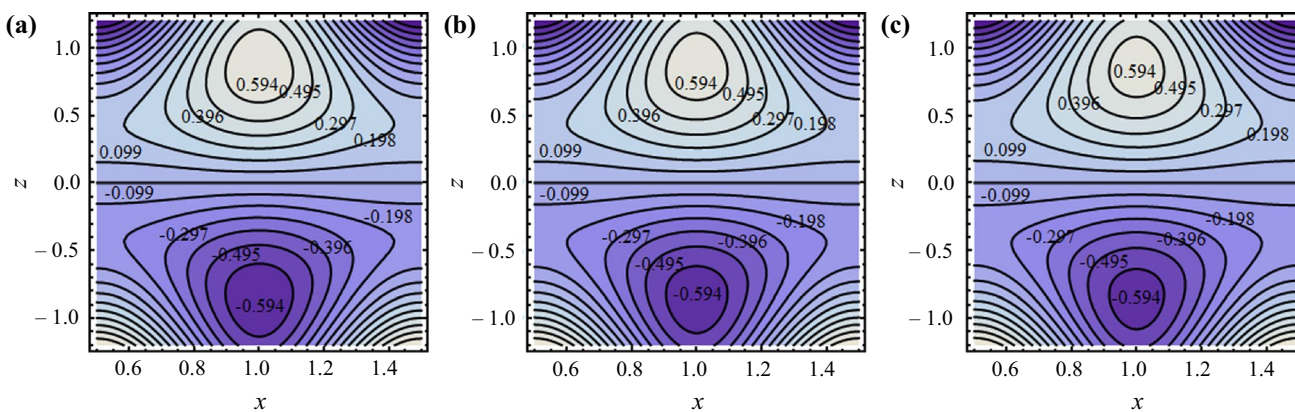


Fig. 19 Streamlines against  $K$

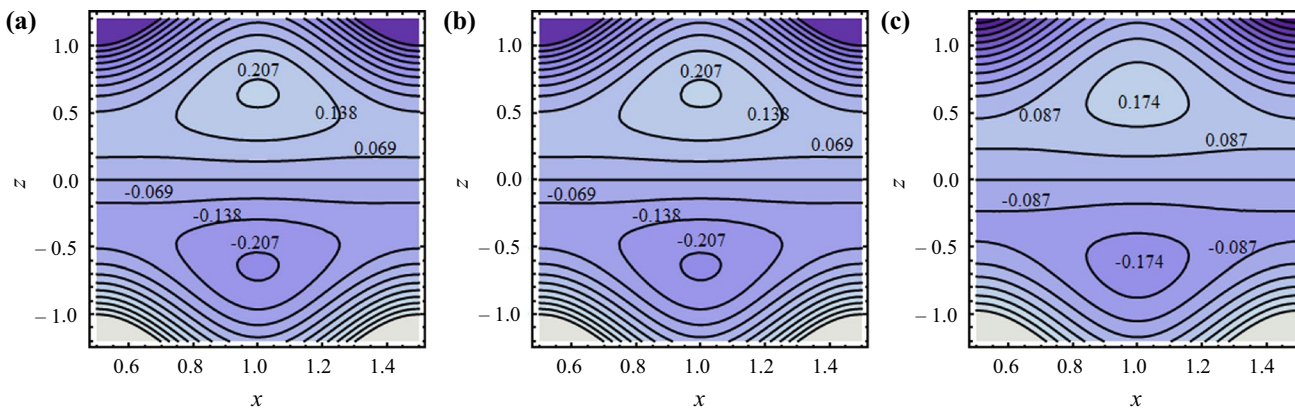


Fig. 20 Streamlines against  $M_1$

**Table 1** Data of velocity profile

| $z$   | For Newtonian fluid | For Eyring–Powell fluid<br>$K = 0.9, M_1 = 0.1$ | $K = 0.9, M_1 = 0.8$ |
|-------|---------------------|---|----------------------|
| – 1.1 | – 1.0000            | – 1.0000  | – 1.0000             |
| – 0.9 | – 0.2884            | – 0.3092  | – 0.3011             |
| – 0.7 | 0.41306             | 0.37308   | 0.38863              |
| – 0.5 | 1.02176             | 0.96587   | 0.98760              |
| – 0.3 | 1.46889             | 1.40163   | 1.42779              |
| – 0.1 | 1.70528             | 1.63208   | 1.66055              |
| 0.10  | 1.70528             | 1.63208   | 1.66055              |
| 0.30  | 1.46889             | 1.40163   | 1.42779              |
| 0.50  | 1.02176             | 0.96587   | 0.98760              |
| 0.70  | 0.41306             | 0.37308   | 0.38863              |
| 0.90  | – 0.2884            | – 0.3092  | – 0.3012             |
| 1.10  | – 1.0000            | – 1.0000  | – 1.0000             |

**Table 2** Variation of temperature factor

| $z$   | For Newtonian fluid | For Eyring–Powell fluid<br>$K = 0.9, M_1 = 0.1$ | $K = 0.9, M_1 = 0.5$ |
|-------|---------------------|---|----------------------|
| – 1.1 | 1.00000             | 1.00000   | 1.00000              |
| – 0.9 | 0.90909             | 0.80161   | 0.76253              |
| – 0.7 | 0.81818             | 0.64255   | 0.57869              |
| – 0.5 | 0.72727             | 0.50755   | 0.42766              |
| – 0.3 | 0.63636             | 0.38969   | 0.29999              |
| – 0.1 | 0.54545             | 0.28589   | 0.19150              |
| 0.10  | 0.45454             | 0.19498   | 0.10059              |
| 0.30  | 0.36363             | 0.11696   | 0.02726              |
| 0.50  | 0.27272             | 0.05301   | – 0.0268             |
| 0.70  | 0.18181             | 0.00619   | – 0.0576             |
| 0.90  | 0.09090             | – 0.0165  | – 0.0556             |
| 1.10  | 0.00000             | 0.00000   | 0.00000              |

**Table 3** Variation of mass concentration

| $z$   | For Newtonian fluid | For Eyring–Powell fluid<br>$K = 0.9, M_1 = 0.1$ | $K = 0.9, M_1 = 0.5$ |
|-------|---------------------|---|----------------------|
| – 1.1 | 1.00000             | 1.00000   | 1.00000              |
| – 0.9 | 0.90909             | 0.74728   | 0.68844              |
| – 0.7 | 0.81818             | 0.50381   | 0.38950              |
| – 0.5 | 0.72727             | 0.28598   | 0.12551              |
| – 0.3 | 0.63636             | 0.10478   | – 0.0885             |
| – 0.1 | 0.54545             | – 0.0329  | – 0.2432             |
| 0.10  | 0.45454             | – 0.1238  | – 0.3341             |
| 0.30  | 0.36363             | – 0.1679  | – 0.3612             |
| 0.50  | 0.27272             | – 0.1685  | – 0.3290             |
| 0.70  | 0.18181             | – 0.1325  | – 0.2468             |
| 0.90  | 0.09090             | – 0.0708  | – 0.1297             |
| 1.10  | 0.00000             | 0.00000   | 0.00000              |

### Conclusions

In the above discussion, the authors have investigated the heat and mass transfer analysis for a viscoelastic fluid model considered in a three-dimensional rectangular peristaltic channel. The problem is handled by collaborative implementation of HPM and eigenfunction expansion method. The flow becomes steady by transforming the observations in a wave frame. The lubrication approach has been made to encounter the laminar flow through small cross sections. The obtained analytical and numerical data have been sketched against different relating coordinates to verify the physical and theoretical effects of many pertinent features of the analysis on velocity component, pressure gradient, pressure rise, thermal and mass profiles. The main points squeezed from the above observations have been labeled below:

1. The velocity profile is becoming larger by aspect ratio of rectangular duct, while it shows opposite facts for Eyring–Powell fluid parameters.
2. It is followed that peristaltic pumping is enhanced by increasing effect of aspect ratio and fluid factors.
3. It is evaluated from the above graphical measures that pressure gradient is varying inversely with aspect ratio and directly with non-Newtonian fluid parameter.
4. The temperature profile and mass concentration give linear behavior with aspect ratio and nonlinear with non-Newtonian features.
5. It is finalized from streamlines that trapping boluses are increasing their numbers with the variation of aspect ratio but remains constant in numbers with the fluid model.

### References

1. Wakif A, Chamkha A, Thumma T, Animasaun IL, Sehaqui R. Thermal radiation and surface roughness effects on the thermomagneto-hydrodynamic stability of alumina-copper oxide hybrid nanofluids utilizing the generalized Buongiorno’s nanofluid model. *J Therm Anal Calorim.* 2020. <https://doi.org/10.1007/s10973-020-09488-z>.
2. Ellahi R, Hussain F, Abbas SA, Sarafraz MM, Goodarzi M, Shadloo MS. Study of two-phase Newtonian nanofluid flow hybrid with Hafnium particles under the effects of slip. *Inventions.* 2020;5:6.
3. Asma M, Othman WA, Muhammad T. Numerical study for Darcy–Forchheimer flow of nanofluid due to a rotating disk with binary chemical reaction and Arrhenius activation energy. *Mathematics.* 2019;7:921.
4. Amanulla CH, Wakif A, Boulahia Z, Reddy MS, Nagendra N. Numerical investigations on magnetic field modeling for Carreau non-Newtonian fluid flow past an isothermal sphere. *J Braz Soc Mech Sci Eng.* 2018;40:462.

5. Nazari S, Ellahi R, Sarafraz MM, Safaei MR, Asgari A, Akbari OA. Numerical study on mixed convection of a non-Newtonian nanofluid in a square cavity with porous media and two lid-driven. *J Therm Anal Calorim.* 2019;140:1121–45.
6. Eid MR, Mahny KL, Dar A, Muhammad T. Numerical study for Carreau nanofluid flow over a convectively heated nonlinear stretching surface with chemically reactive species. *Physica A.* 2020;540:123063.
7. Waqas H, Khan SU, Bhatti MM, Imran M. Significance of bioconvection in chemical reactive flow of magnetized Carreau–Yasuda nanofluid with thermal radiation and second-order slip. *J Therm Anal Calorim.* 2020;140:1293–306.
8. Abolbashari MH, Freidoonimehr N, Nazari F, Rashidi MM. Analytical modeling of entropy generation for Casson nanofluid flow induced by a stretching surface. *Adv Powder Technol.* 2015;26:542–52.
9. Bhatti MM, Rashidi MM. Effects of thermo-diffusion and thermal radiation on Williamson nanofluid over a porous shrinking/stretching sheet. *J Mol Liq.* 2016;221:567–73.
10. Powell RE, Eyring H. Mechanisms for the relaxation theory of viscosity. *Nature.* 1944;154:427–8.
11. Zeeshan A, Ijaz N, Majeed A. Analysis of magnetohydrodynamics peristaltic transport of hydrogen bubble in water. *Int J Hydrogen Energy.* 2018;43:979–85.
12. Raza M, Ellahi R, Sait SM, Sarafraz MM, Shadloo MS, Waheed I. Enhancement of heat transfer in peristaltic flow in a permeable channel under induced magnetic field using different CNTs. *J Therm Anal Calorim.* 2020;140:1277–91.
13. Ramesh K, Prakash J. Thermal analysis for heat transfer enhancement in electroosmosis-modulated peristaltic transport of Sutterby nanofluids in a microfluidic vessel. *J Therm Anal Calorim.* 2019;138:1311–26.
14. Reddy S, Mishra M, Sreenadh S, Rao RA. Influence of lateral walls on peristaltic flow in a rectangular duct. *J Fluids Eng.* 2005;127:824–7.
15. Mekheimer KS, Abdellateef AI. Peristaltic transport through eccentric cylinders: mathematical model. *Appl Bion Biomech.* 2013;10:19–27.
16. Aranda V, Cortez R, Fauci L. Stokesian peristaltic pumping in a three-dimensional tube with a phase-shifted asymmetry. *Phys Fluids.* 2011;23:081901.
17. Aranda V, Cortez R, Fauci L. A model of Stokesian peristalsis and vesicle transport in a three-dimensional closed cavity. *J Biomech.* 2015;48:1631–8.
18. Abbas MA, Bai YQ, Bhatti MM, Rashidi MM. Three dimensional peristaltic flow of hyperbolic tangent fluid in non-uniform channel having flexible walls. *Alex Eng J.* 2016;55:653–62.
19. Nadeem S, Akbar NS, Bibi N, Ashiq S. Influence of heat and mass transfer on peristaltic flow of a third order fluid in a diverging tube. *Commun Nonlinear Sci Numer Simul.* 2010;15:2916–31.
20. Srinivas S, Kothandapani M. The influence of heat and mass transfer on MHD peristaltic flow through a porous space with compliant walls. *Appl Math Comput.* 2009;213:197–208.
21. Ogulu A. Effect of heat generation on low Reynolds number fluid and mass transport in a single lymphatic blood vessel with uniform magnetic field. *Int Commun Heat Mass Transf.* 2006;33:790–9.
22. Mekheimer KS. The influence of heat transfer and magnetic field on peristaltic transport of a Newtonian fluid in a vertical annulus: application of an endoscope. *Phys Lett A.* 2008;372:1657–65.
23. Ji-Huan HE. A note on the homotopy perturbation method. *Therm Sci.* 2010;14:565–8.
24. He JH. Homotopy perturbation method for solving boundary value problems. *Phys Lett A.* 2006;350:87–8.

**Publisher's Note** Springer Nature remains neutral with regard to jurisdictional claims in published maps and institutional affiliations.